Journal of Applied Physics

RESEARCH ARTICLE | FEBRUARY 12 2025

Monte Carlo study of the electron emission yields of germanium

H. I. Imtiaz ; Y. B. Zou ; S. F. Mao ; M. S. S. Khan; Z. J. Ding

J. Appl. Phys. 137, 065105 (2025)
https://doi.org/10.1063/5.0251814

Journal of Applied Physics ARTICLE pubs.aip.org/aip/jap

Monte Carlo study of the electron emission yields of germanium

Cite as: J. Appl. Phys. **137**, 065105 (2025); doi: 10.1063/5.0251814
Submitted: 5 December 2024 · Accepted: 27 January 2025 ·
Published Online: 12 February 2025

H. I. Imtiaz,[1] Y. B. Zou,[2,a)] S. F. Mao,[3] M. S. S. Khan,[4] and Z. J. Ding[1,5,a)]

AFFILIATIONS

[1]Department of Physics, University of Science and Technology of China, Hefei, Anhui 230026, People's Republic of China
[2]School of Physics & Electronic Engineering, Xinjiang Normal University, Urumqi, Xinjiang 830054, People's Republic of China
[3]School of Nuclear Science and Technology, University of Science and Technology of China, Hefei, Anhui 230026, People's Republic of China
[4]Key Laboratory of Materials Physics, Institute of Solid State Physics, Chinese Academy of Sciences, Hefei, Anhui 230031, People's Republic of China
[5]Hefei National Research Center for Physical Sciences at the Microscale, University of Science and Technology of China, Hefei, Anhui 230026, People's Republic of China

[a)]**Authors to whom correspondence should be addressed:** zouyb@xjnu.edu.cn and zjding@ustc.edu.cn

ABSTRACT

Though extensive experiments have been performed in the past to measure electron emission properties under electron beam bombardment, reliable measured data for clean and smooth surfaces are still lacking for most elemental solids. In this study, we have conducted a comprehensive Monte Carlo simulation to examine electron emission yields, including secondary electron yield (SEY), backscattering coefficient (BSC), and total electron yield (TEY), for germanium. The uncertainties associated with theoretical calculations have also been assessed with a total of 4608 scattering models by considering several dominant factors that can influence the calculated yields, i.e., optical energy loss function dataset, work function data, dielectric function model for electron inelastic scattering, and scattering potential for electron elastic scattering. Our results indicate that the work function value significantly affects the simulated SEY, and the energy loss function dataset and elastic scattering potential moderately influence both SEY and BSC. Our simulated BSC data are somewhat higher than most of the experimental measurements, while the simulated SEY data are mostly lower than the experimental data within the estimated theoretical uncertainty. This study highlights the critical need for establishing an accurate database of electron emission yields using theoretical modeling, considering particularly the unreliability of the previous experimental data caused by surface contamination during measurements.

I. INTRODUCTION

Interaction of energetic ions or electrons with materials can produce the secondary electron emission. Austin and Starke[1] were the pioneers who discovered the secondary electron emission; afterward, many studies have been performed experimentally or theoretically. Nowadays, secondary electron emission has numerous applications in various technical fields, e.g., scanning electron microscopy (SEM)[2] and electron multipliers.[3] It also plays a fundamental role in lithography technique,[4] fabrication of electronic devices,[5] electron accelerator,[6] and microwave devices.[7] In vacuum electronic devices, one wishes to either enhance or suppress the secondary electron emission intensity measured as the secondary electron yield (SEY).

The incident electrons undergo elastic and inelastic collisions in the material. A fraction of them will be reflected elastically from the solid surface without losing their primary energy, while many others will suffer energy losses inside the solid and result in secondary electron production. These generated secondary electrons can start cascade processes of the next generation of secondary electrons. In the end, these excited secondary electrons will either rejoin the conduction electrons by losing most of their kinetic energies or emit from the surface if they still have sufficient energy to

overcome the surface potential barrier when reaching the surface region. Conventionally, emitted low energy electrons having energies below 50 eV are termed as true secondary electrons, while those with energies greater than 50 eV are counted as backscattered electrons.[8] The ratio between the number of true secondary electrons and the number of incident electrons is defined as the SEY (δ), while the similar ratio between the number of backscattered electrons and the number of incident electrons is the backscattering coefficient (BSC, η).

It has been well known that the surface chemical and physical states, mostly the surface cleanness and roughness, influence SEY significantly; a vast literature has already been dedicated to this study.[9–11] This fact also can be clearly seen from an experimental database of SEY and BSC collected for historically measured values by various research groups.[12] A very high divergence is usually found for many elemental solids investigated so far. For example, for Al, Cu, Ag, and Au, the variation in the maximum SEY (δ_m) among the measured values can be as large as ~240%, 150%, 60%, and 50%, respectively. This extent of variation hinders one to derive a reliable absolute yield curve, i.e., the $\delta(E_p)$-relationship where E_p represents the primary energy of incident electrons; hence, a reduced fitting curve $\delta(E_p/E_{pm})/\delta_m$ where E_p represents the primary energy corresponding to δ_m was considered instead and the curve shape was found universal for most of the materials.[13,14] Although a machine learning method has recently been applied to the updated SEY database[15] aiming to combine the physical and chemical properties of elements in the periodic table to find the absolute yield curve, it must be noted that the accuracy of the derived expression is subject to the accuracy of the original experimental data. The systematic error involved in the measured data cannot be eliminated by the machine learning method.

Regarding the measured BSC data a very good agreement was found between various measurements and for many elements but only at very high primary energies, usually ~100 keV.[16] Below 10 keV, the discrepancy among the measured data becomes very significant with decreasing primary energy. For example, for Be, Mo, and W, the variation of η at 1 keV among the measured values is as high as 57%, 63%, and 40%, respectively.[17,18] Despite the discrepancy, Reuter's empirical fitting formula derived from the measured data for normal incidence of 20 keV beam,[2] $\eta = -0.0254 + 0.016Z - 1.86 \times 10^{-4}Z^2 + 8.3 \times 10^{-7}Z^3$, where Z is the atomic number, has been used widely. The reason for the discrepancy has long been rarely discussed until fairly recently by theoretical studies with a comprehensive Monte Carlo simulation. It is explored that the surface contamination during the measurements is very likely the key responsible reason for the scattered BSC data measured at low primary energies.[17–19] Therefore, both the measured SEY and BSC values can be well influenced by the sample properties, which are determined by the vacuum condition and surface cleaning technique. The historical data in the database[12] collected without discriminating surface state, which was rarely quantified or even described in an old publication, may suffer significant systematic measurement error and, hence, are not reliable for use.

On the other hand, Monte Carlo simulation methods[20–23] have been developed for applications to various electron beam techniques including electron probe microanalysis,[24,25] electron beam lithography,[26–28] scanning electron microscopy,[29–33] electron spectroscopy,[34–36] and radiation research.[37] In these simulations, backscattered electrons and secondary electrons are either the interested output signals or typical variables for model validation. Through immense theoretical attempts devoted lasting over half century,[38–47] a very accurate Monte Carlo physical modeling has now been established, with which the electron elastic scattering resulted from electron–nucleus interaction and electron inelastic scattering from electron–electron interaction can be accurately described by the Mott cross section and dielectric function, respectively.[48–50] In particular, Penn's algorithm has enabled one to derive, although approximately in formulation but very efficiently in computation, the momentum transfer- and frequency-dependent dielectric function, $\varepsilon(q, \omega)$, from the experimentally measured data of optical dielectric function, $\varepsilon(q = 0, \omega)$,[51] or the optical energy loss function (ELF), $\mathrm{Im}\{-1/\varepsilon(0, \omega)\}$. The accuracy of such Monte Carlo modeling has been confirmed by comparing the calculated energy spectrum of backscattered electrons and the simulated electron emission yields with experiments.[52,53] The main advantage of this up-to-date Monte Carlo model over the early approaches based on the continuous slowing down approximation[41,42] lies in the fact that it has enabled the simulation of individual electron scattering events free of fitting parameters. In addition, in general the use of experimental dielectric function, or the optical constants,[54] in the Monte Carlo physical modeling replicates more exactly the electronic excitation happened in a realistic material than the full *ab initio* approach with the first-principles computation except for a few cases.[55]

The weakness of this Monte Carlo modeling with the optical ELF is that for many materials, the optical constants measured in a wide frequency range are still lacking. Furthermore, the compiled data of optical constants measured with optical methods[54] often suffer some defects, i.e., missing data in some frequency ranges and/or having the unsatisfactory data accuracy tested by the sum rules. A recent study has indicated that the accuracy of the ELF data can, indeed, influence the calculated BSC values to a considerable extent.[56] Fortunately, in recent years, a reverse Monte Carlo technique has been developed to derive the optical constants in a wide frequency range or the energy loss range up to ~200 eV from the experimentally measured reflection electron energy loss spectroscopy (REELS) spectra.[57–69] It is then highly expected that a more accurate optical constants database based on electron beam technique will be constructed in the near future, at least for elemental solids. Therefore, with such continuous efforts toward improving modeling accuracy, the role of the Monte Carlo simulation method for the study of electron–matter interaction has come to the turning point that it can help to validate experimental measurement other than the opposite previously.

The reliable modeling of electron–matter interaction, therefore, enables the electron emission yields for ideal clean and smooth surfaces to be obtained for establishing a compact and accurate theoretical database. In order to do so, more studies concerning the theoretical uncertainty have to be done first. The process of characterizing, identifying, and quantifying those aspects that can influence a simulation output is uncertainty quantification. It is involved in an extensive range of simulations for many engineering and scientific problems.[70–72] At present, different research

areas and modeling domains are already implementing the uncertainty quantification standard at different levels; the modeling data will be judged as imperfect without evaluating the related uncertainties. In the case of Monte Carlo simulation of electron–matter interaction, there has not been much work done on uncertainty quantification till now, and the main reason for the partial attention of researchers toward the uncertainty quantification of Monte Carlo simulation might be the high cost required for the computation. In this work, we have considered a number of factors that can affect the simulated SEY and BSC values and evaluated the simulation uncertainties.

A particular Monte Carlo simulation method/code is based on the combination of the physical modeling of electron scattering and the simulation algorithm, which is the set of numerical procedures used to generate electron trajectories.[25] The combined standard uncertainty of the simulation result can then be expressed as, $u^2_{\text{simulation}} = u^2_{\text{modelling}} + u^2_{\text{numerical}} + u^2_{\text{specimen}}$, where u_{modeling}, $u_{\text{numerical}}$, and u_{specimen} are the uncertainties due to physical modeling, numerical calculation, and specimen factors for the geometrical structure of the sample, respectively.[33] As discussed previously,[18] the uncertainty term $u_{\text{numerical}}$ is negligible here. The uncertainty term due to the specimen, u_{specimen}, includes the geometrical, physical, and chemical factors that can influence the simulation result. Here, we put the physical and chemical factors into the $u_{\text{modelling}}$ term, and the geometrical factor is null because the sample is structure less, or more precisely, we deal with the ideal planar surface. Then, the uncertainty $u_{\text{modelling}}$ is the sole term involved in the evaluation.

Although it has been recognized that the most accurate models for elastic and inelastic scattering are Mott's cross section and dielectric functional theory, respectively, there are still uncertainties involved in the inputs of a Monte Carlo simulation at the moment. For elastic scattering, a number of interaction potential models are available and there is no established criterion to select the best one. For electron inelastic scattering, several optical ELF datasets from different sources are usually available,[54,73] and, if there is no much difference between the sum rules, the optical ELF will be an uncertainty factor. Although this factor will disappear in future with the increasing accuracy of the ELF data measured by REELS, it is still necessary at present to include it. Additionally, some physical parameters, such as mass density and work function, will also contribute to the uncertainty when modeling a practical sample. For example, an experimentally prepared amorphous material often has varied density values. The work function value is usually distributed in a range in literature studies;[74] in addition, the surface contamination would alter not only the surface chemical environment but also the work function, which, in turn, results in the change in the electron emission yield.[75,76]

In this work, the uncertainties related to physical modeling together with experimental input data are investigated. In our investigation, we have considered different scattering potential models for electron elastic scattering. The effect of work function and energy loss function data is also taken into consideration. Here, we investigate a semiconductor material, Ge, for the uncertainty quantification of electron emission due to the following reasons: the practical applications of Ge are in a broad range; there are different optical constants datasets and work function values. Furthermore, the measured SEY and BSC data have quite large variation.

II. THEORETICAL MODELING

In this work, we utilize our up-to-date Monte Carlo code, CTMC-SEM.[17] This code is able to perform the simulation of primary and cascade secondary electron trajectories in a bulk target to predict electron emission yields.

A. Elastic scattering

Mott's cross section has been commonly used to precisely calculate electron elastic scattering even at low electron energies. The differential cross section is given as[77]

$$\frac{d\sigma_e}{d\Omega} = |f(\theta)|^2 + |g(\theta)|^2, \tag{1}$$

where $f(\theta)$ and $g(\theta)$ represent the scattering amplitudes expressed by the partial wave expansion as

$$f(\theta) = \frac{1}{2ik}\sum_{l=0}^{\infty}\{(\ell+1)(e^{2i\delta_\ell^+} - 1) + \ell(e^{2i\delta_\ell^-} - 1)\}P_\ell(\cos\theta), \tag{2}$$

$$g(\theta) = \frac{1}{2ik}\sum_{\ell=1}^{\infty}\{-e^{2i\delta_\ell^+} + e^{2i\delta_\ell^-}\}\,P_\ell^1(\cos\theta), \tag{3}$$

where δ_l^+ and δ_l^- represent the phase shifts for spin up and spin down of the ℓth partial wave, respectively. $P_\ell(\cos\theta)$ is the Legendre function, and $P_\ell^1(\cos\theta)$ is the first-order associated Legendre function. The phase shifts are computed from a radial equation describing electron transport in an atomic potential field,

$$V(r) = V_{\text{st}}(r) + V_{\text{ex}}(r) + V_{\text{cp}}(r) - iW_{\text{abs}}(r), \tag{4}$$

where r is the distance between the electron and the atomic nucleus. $V_{\text{st}}(r)$, $V_{\text{ex}}(r)$, and $V_{\text{cp}}(r)$ represent the electrostatic potential, exchange potential, and correlation-polarization potential, respectively. $W_{\text{abs}}(r)$ is the imaginary absorption potential, which is regarded as zero here. The selection of potential models is one of the main factors contributing to the uncertainty quantification.

Salvat's latest version of ELESPA[78] with additional functionality has been used to calculate the differential and total elastic cross sections. In ELSEPA, the default model is for free atoms, while in this work, we have considered both muffin-tin potential and free atom potential. A combination of four electron exchange potential models, four nuclear charge distribution models, four electron distribution models, and three models of correlation polarization potential then resulted in a total of 384 (=2 × 4 × 4 × 4 × 3) distinct scattering potentials (see Ref. 17 Table A1) and their associated cross section datasets; in comparison with one of our previous works, totally 192 (=4 × 4 × 4 × 3) scattering potential models were included.[19] Figure 1 shows the elastic mean free paths in a Ge solid calculated from the 384 Mott's total cross section datasets. One can find a large variation among them in the whole energy range, particularly in the lower energy region. The variation extent is much more prominent than

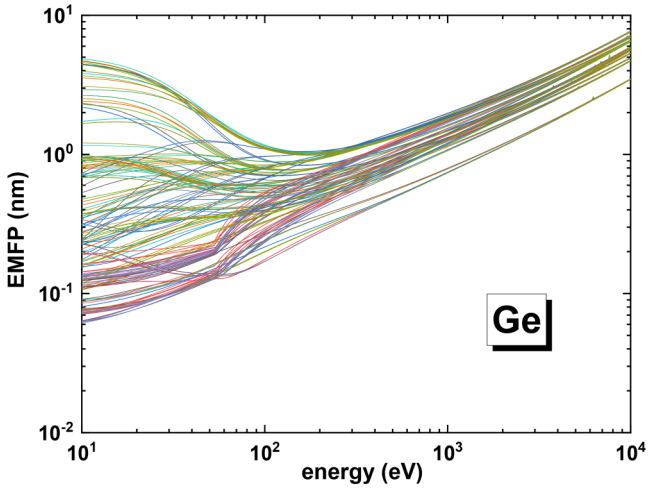

FIG. 1. Calculated elastic mean free paths for 384 different elastic scattering cross section datasets for Ge using the ELSEPA code.

that of a similar semiconductor, Si,[79] because of the difference in the atomic number. It can, thus, be predicted that the uncertainty of SEY for Ge would be greater than the case of Si.

B. Inelastic scattering

Coulomb's interaction between a kinetic electron and atomic electrons results in electron inelastic scattering with which the kinetic electron loses an energy to cause electronic excitation. The dielectric functional approach provides a unified description of the core- and valence-electron excitations in terms of the dielectric function of the medium. The differential inverse inelastic mean free path is given as[80]

$$\frac{d^2\lambda_{in}^{-1}}{d(\hbar\omega)dq} = \frac{2}{1+\gamma}\frac{1}{\pi a_0(E-E_g)}\mathrm{Im}\left[\frac{-1}{\varepsilon(q,\omega)}\right]\frac{1}{q}, \tag{5}$$

where λ_{in} is the electron inelastic mean free path (IMFP), E_g is the bandgap of the material,$\gamma = 1 + (E - E_g)/m_e c^2$ is the relativistic correction factor, m_e is the electron rest mass, and a_0 is the Bohr radius. $\mathrm{Im}\{-1/\varepsilon(q,\omega)\}$ is the momentum transfer ($\hbar q$)–energy loss ($\hbar\omega$)-dependent ELF, which determines the probability of an inelastic scattering event. In the above equation, the kinetic energy E of an electron is referenced to the bottom of the valence band. For Ge, the bandgap is $E_g \simeq 0.7$ eV and the valence bandwidth is $E_v \simeq 12.6$ eV.

The conduction electrons are excited in two ways, i.e., collective excitation and single-particle excitation.[81,82] In the case of a free electron metal, they can be precisely characterized by the Lindhard dielectric function.[82,83] However, in general, the dielectric function is hard to obtain theoretically for a non-free electron material. In addition, the accuracy of *ab initio* calculation of dielectric function is still limited, particularly, for large energy losses (higher than several tens eV) and heavy elements. Therefore, it has been suggested to use the experimentally measured optical constants or optical dielectric function $\varepsilon(\omega)$ at long wavelength limit $q \to 0$ to derive approximately the q-dependent ELF.[84] Penn has further proposed a formalism for the extension of optical ELF to the q-dependent ELF.[51] According to this full Penn algorithm (FPA), the optical ELF, $\mathrm{Im}\{-1/\varepsilon(\omega)\}$, is extended into the (q, ω)-plane with an expansion according to the Lindhard ELF as

$$\mathrm{Im}\left\{\frac{-1}{\varepsilon(q,\omega)}\right\} = \int_0^\infty d\omega_p g(\omega_p)\mathrm{Im}\left\{\frac{-1}{\varepsilon_{\mathrm{L}}(q,\omega;\omega_p)}\right\}, \tag{6}$$

where the expansion coefficient is given as

$$g(\omega) = \frac{2}{\pi\omega}\mathrm{Im}\left\{\frac{-1}{\varepsilon(\omega)}\right\}. \tag{7}$$

Here, the Lindhard dielectric function for free electron gas having plasmon energy $\hbar\omega_p$ is represented by $\varepsilon_{\mathrm{L}}(q,\omega;\omega_p)$; its real and imaginary parts are given by, respectively,

$$\varepsilon_{\mathrm{L}}^{\mathrm{r}} = 1 + \frac{2}{\pi a_0 q}\frac{1}{Z}\left[\frac{1}{2} + \frac{1}{8Z}F\left(Z - \frac{X}{4Z}\right) + \frac{1}{8Z}F\left(Z + \frac{X}{4Z}\right)\right], \tag{8}$$

and

$$\varepsilon_{\mathrm{L}}^{\mathrm{i}} = \begin{cases} \dfrac{1}{8a_0k_{\mathrm{F}}}\dfrac{X}{Z^3}, & 0 \le X \le 4Z(1-Z), \\ \dfrac{1}{8a_0k_{\mathrm{F}}}\dfrac{1}{Z^3}\left[1 - \left(Z - \dfrac{X}{4Z}\right)^2\right], & |4Z(1-Z)| \le X \le 4Z(1+Z), \\ 0, & \text{otherwise}, \end{cases} \tag{9}$$

where $X = \hbar\omega/E_{\mathrm{F}}$, $F(x) = (1-x^2)\ln|(x+1)/(x-1)|$, $Z = q/2k_{\mathrm{F}}$. $E_{\mathrm{F}} = \hbar^2k_{\mathrm{F}}^2/2m$ and k_F are the Fermi energy and Fermi wave vector, respectively.

Alongside the plasmon dispersion line, Lindhard ELF is the δ-function where $\varepsilon_{\mathrm{L}}^{\mathrm{r}} = 0$ and $\varepsilon_{\mathrm{L}}^{\mathrm{i}} = 0$ is equal to zero. The calculation is then carried out separately for the plasmon and single electron excitation components,

$$\mathrm{Im}\left\{\frac{-1}{\varepsilon(q,\omega)}\right\}_{\mathrm{FPA}} = \mathrm{Im}\left\{\frac{-1}{\varepsilon(q,\omega)}\right\}_{\mathrm{e}} + \mathrm{Im}\left\{\frac{-1}{\varepsilon(q,\omega)}\right\}_{\mathrm{pl}}. \tag{10}$$

It is simple to calculate the single excitation component as

$$\mathrm{Im}\left\{\frac{-1}{\varepsilon(q,\omega)}\right\}_{\mathrm{e}} = \int_0^\infty d\omega_p g(\omega_p)\mathrm{Im}\left\{\frac{-1}{\varepsilon_{\mathrm{L}}(q,\omega;\omega_p)}\right\} \Theta[q^+(\omega;\omega_p) - q]\Theta[q - q^-(\omega;\omega_p)], \tag{11}$$

where

$$\begin{cases} q^{-}(\omega;\omega_p) = -k_{\mathrm{F}}(\omega_p) + \sqrt{k_{\mathrm{F}}^2(\omega_p) + 2m\omega/\hbar}, \\ q^{+}(\omega;\omega_p) = k_{\mathrm{F}}(\omega_p) + \sqrt{k_{\mathrm{F}}^2(\omega_p) + 2m\omega/\hbar}, \end{cases} \tag{12}$$

are the area's left and right limits when $\varepsilon_{\mathrm{L}}^{\mathrm{i}} \neq 0$.

The plasmon excitation component can be computed as

$$\mathrm{Im}\left\{\frac{-1}{\varepsilon(\omega,q)}\right\}_{\mathrm{pl}} = g(\omega_p)\frac{\pi}{|d\varepsilon_{\mathrm{L}}^{\mathrm{r}}(q,\omega;\omega_p)/d\omega_p|}\Big|_{\varepsilon_{\mathrm{L}}^{\mathrm{r}}(q,\omega;\omega_p)=0}\Theta[q^{-}(\omega;\omega_p) - q], \tag{13}$$

while the Lindhard dielectric function's slop for the real part near the plasmon dispersion line is expressed as

$$\begin{aligned} & d\varepsilon_{\mathrm{L}}^{\mathrm{r}}(q,\omega;\omega_p)/d\omega_p|_{\varepsilon_{\mathrm{L}}^{\mathrm{r}}(q,\omega;\omega_p)=0} \\ &= -\frac{2}{3\omega_{\mathrm{p}}}\left\{2 + \frac{1}{\pi a_0 q}\frac{1}{Z} + \frac{1}{2\pi a_0 q}\frac{1}{Z}\right. \\ &\times\left[2 - C_1 \ln\left|\frac{C_1+1}{C_1-1}\right| - C_2 \ln\left|\frac{C_2+1}{C_2-1}\right|\right. \\ &\left.\left. + \frac{X}{4Z^2}\left(C_1 \ln\left|\frac{C_1+1}{C_1-1}\right| - C_2 \ln\left|\frac{C_2+1}{C_2-1}\right|\right)\right]\right\}, \end{aligned} \tag{14}$$

whereas $C_1 = Z - X/4Z$ and $C_2 = Z + X/4Z$.

C. Energy loss function

The inelastic interaction is a fundamental mechanism during the electron transport process in a material that leads to the generation of secondary electrons. As a result, the simulated electron emission yields are affected by the quality of the optical ELF data as a crucial input to our Monte Carlo simulation. Palik has collected the measured optical constants for a number of elemental solids and compounds from multiple sources to construct a database,[54] where the photon energy $\hbar\omega$ is ranged from sub-eV to over keV. Recent studies of REELS have provided an additional database of optical constants where the energy loss $\hbar\omega$ is ranged from ~1 eV to 50–200 eV.[57–68,73] At high photon energies, additional databases are available.[85,86] The combinations of them give four ELF datasets for Ge, as illustrated in Fig. 2, which are named "Present," "Novak," "Marton," and "Yang." Table I shows the data components for the four ELF datasets in detail. The involved data are taken from several sources, including Palik,[54] Novák *et al.*[87] Marton and Toots,[88] Yang *et al.*,[62] and Henke *et al.*[85] Below 2 eV, the dataset of "Yang" was simply estimated by a straight line in a log–log plot so that the electronic and phonon excitations below 2 eV are poorly described. Therefore, the dataset of "Present" for $\hbar\omega < 2$ eV uses the data measured by the optical method instead, having more accurate description around and below the bandgap.

Two sum rules, the perfect-screening sum rule and the oscillator strength sum rule, for optical constants[90] are used to test the accuracy of the datasets. They constitute the limiting form of Kramers–Kronig integral.[91] The *f*-sum rule is

$$Z_{\mathrm{eff}} = \frac{2}{\pi\,\Omega_p^2}\int_0^{\omega_{\max}} \omega\mathrm{Im}\left\{\frac{-1}{\varepsilon(\omega)}\right\}d\omega, \tag{15}$$

where $\hbar\Omega_P = \sqrt{4\pi n_a e^2/m}$. Once $\omega_{\max} \to \infty$, the expected value of Z_{eff} has to be the atomic number of the element for an elemental solid. The *ps*-sum rule is

$$P_{\mathrm{eff}} = \frac{2}{\pi}\int_0^{\omega_{\max}} \frac{1}{\omega}\mathrm{Im}\left\{\frac{-1}{\varepsilon(\omega)}\right\}d\omega + \mathrm{Re}\left\{\frac{-1}{\varepsilon(0)}\right\}. \tag{16}$$

In the case of conductors $\mathrm{Re}\{1/\varepsilon(0)\} = 0$. For non-conductors, the value of refractive index n is greater than the extinction coefficient k at lower frequencies. Therefore, $\mathrm{Re}\{-1/\varepsilon(0)\} \simeq 1/n^2(0)$. $n(0) = 4.0043$ is used to calculate P_{eff} for Ge. The value of P_{eff} should be equal to unity, once $\omega_{\max} \to \infty$. By the ω-factor in Eq. (15), the high photon energy region of ELF dominates the accuracy of the *f*-sum rule. On the other hand, the low photon energy region for phonon scattering and valence-electron excitation dominates the accuracy of the *ps*-sum rule, due to the ω^{-1}-factor in Eq. (16). While this is merely an overall justification, it is impossible to evaluate accuracy in a given photon energy range.

Table II displays the *f*-sum rule and *ps*-sum rule, along with their relative errors, for the four ELFs under consideration. The sum rule plot is shown in Fig. 3. Each ELF has different sum rule values. The relative errors of *f*-sum rule are satisfactory for "ELF-Yang" and "ELF-Present," being below 1%, while their relative errors for *ps*-sum rule are somewhat larger. For "ELF-Marton" and "ELF-Novak," in comparison, the *f*-sum rule error is larger and the *ps*-sum rule error is smaller. By overall evaluation, the four

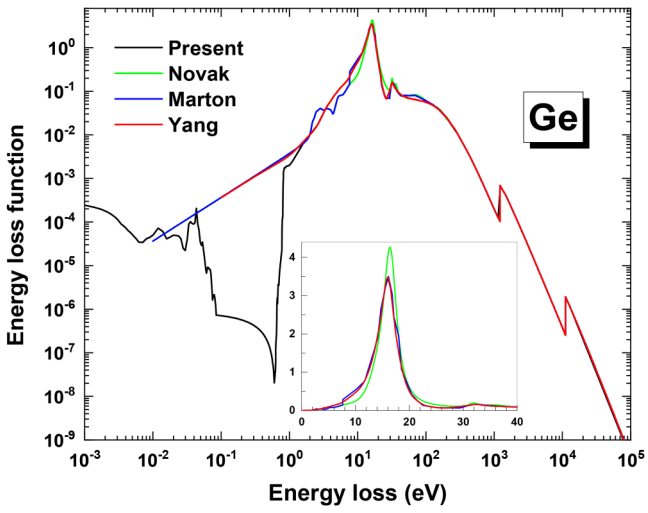

FIG. 2. Comparison of the four ELFs adopted for the Monte Carlo simulation.

TABLE I. The optical ELF data used for Ge.

ELF	Photon energy range and the corresponding dataset				
Present	0.001–2 eV[54]		2–200 eV[62]		
Novak		0.01–200 eV[87]			
Marton	0.01–7.66 eV[87]		7.66–200 eV[88]	200–2000 eV[89]	2000–10 000 eV[85]
Yang		0.1–200 eV[62]			

datasets have no big difference in accuracy and the "ELF-Present" and "ELF-Yang" datasets may be better.

Figure 4 compares the computed IMFP curves calculated by the FPA model with the four distinct ELF datasets. It shows that the four IMFP curves are very close to one another. In particular, the "IMFP-Yang" curve and "IMFP-Present" curve agree. Below 50 eV, "IMFP-Novak" is higher than the other three IMFP curves, while above 50 eV, it is slightly lower. The difference of IMFP curves corresponding to four optical ELFs follows the sum rule results of the ELFs reported in Table II. Because the *ps*-sum rules for "ELF-Present" and "ELF-Yang" are underestimated, while the *f*-sum rules for "ELF-Present" and "ELF-Yang" are quite reasonable, the resultant "IMFP-Present" and "IMFP-Yang" would be slightly overestimated in the low energy region. Comparatively, the *f*-sum rule for "ELF-Novak" is overestimated, and the resultant "IMFP-Novak" curve is underestimated in the high energy region. Previous calculations on BSCs for specific metals utilizing different ELF datasets, in which the sum rule errors are different, have already demonstrated that sum rules can describe well the disparity between the computed BSCs of different ELFs.[56] The electron emission yields can be influenced by the ELF input data because distinct ELFs produce different IMFPs depending on energy.

D. Secondary electron generation

An electron may reach the surface for emission following a series of elastic and inelastic collisions within the sample. A quantum mechanical transmission coefficient[92] is used to determine whether the electron will reflect or refract from the surface,

$$T(E,\beta)=\begin{cases}\dfrac{4\sqrt{1-U_0/E\cos^2\beta}}{\left[1+\sqrt{1-U_0/E\cos^2\beta}\right]^2}, & \text{if } E\cos^2\beta > U_0,\\ 0, & \text{otherwise,}\end{cases} \tag{17}$$

where β represents the angle between the traveling electron's direction and the surface normal. U_0 represents the surface potential barrier. In this study, the reference level for the electron kinetic energy E in the Monte Carlo simulation is the vacuum level and the bottom of the conduction band of an insulator or semiconductor when an electron is in vacuum or material, respectively. Therefore, when an electron penetrates the surface from either the bulk or vacuum side, its kinetic energy is changed according to the reference level. From Eq. (17), it can be seen that the SEY is greatly influenced by the surface barrier value. The work function can be experimentally measured with a variety of methods, including the photoelectric, effusion, thermionic, contact potential difference, calorimetric, and field-emission methods. The measured work function for Ge ranges from 3.52 to 4.83 eV. In the simulation, we utilized this range for uncertainty range evaluation.

TABLE II. The relative errors of the *f*- and *ps*-sum rules for Ge.

	f-sum		*ps*-sum	
ELF	Value	Relative error (%)	Value	Relative error (%)
Present	32.206	0.64%	0.935	−6.40%
Novak	33.228	3.83%	0.942	−5.70%
Marton	32.891	2.78%	0.968	−3.13%
Yang	32.206	0.64%	0.937	−6.23%

III. UNCERTAINTY QUANTIFICATION

Once a functional formula for the given variables is provided, the uncertainty propagation resulting from their uncertainty can be calculated analytically. The overall standard uncertainty for a function $y=f(x_1, x_2, \ldots x_N)$ is expressed as $u_y^2=\sum_{i=1}^{N}(\partial f/\partial x_i)^2 u_{x_i}^2$ for the measured y, where u_{x_i} represents the uncertainty of the ith input quantity.[93] Although in the current scenario, it is not possible to provide an explicit functional dependence of electron emission yields on the concerned variables (elastic scattering cross section, ELF data, and work function). So, in order to assess the uncertainty propagation, we used Monte Carlo uncertainty quantification.[94,95] Defining the probability density functions for input quantities and then starting the Monte Carlo simulation are the main steps in the approach. The simulation will give the output distribution, as well as the output's uncertainty. A detailed description of the flow chart used in the current theoretical computation of electron emission yields and the associated uncertainty quantification can be found in our previous work.[79] Monte Carlo simulation process for estimating the theoretical uncertainty of electron emission yields starts with the simulation for a specified number of iterations M, whereas the main input parameters are work function, energy loss function (ELF), and scattering potential. To check the uncertainty due to a specific parameter, we kept all other parameters constant and ran Monte Carlo computation, which itself contains step by step tracking of electron trajectories within the material. The output data provide electron emission yields and the corresponding uncertainties.

The probability density function for each uncertain variable is assumed uniform in this work. For every incident energy, a series of Monte Carlo trials for $M=4608$ scattering models (384 elastic scattering potentials, 4 ELF datasets, and 3 work function values)

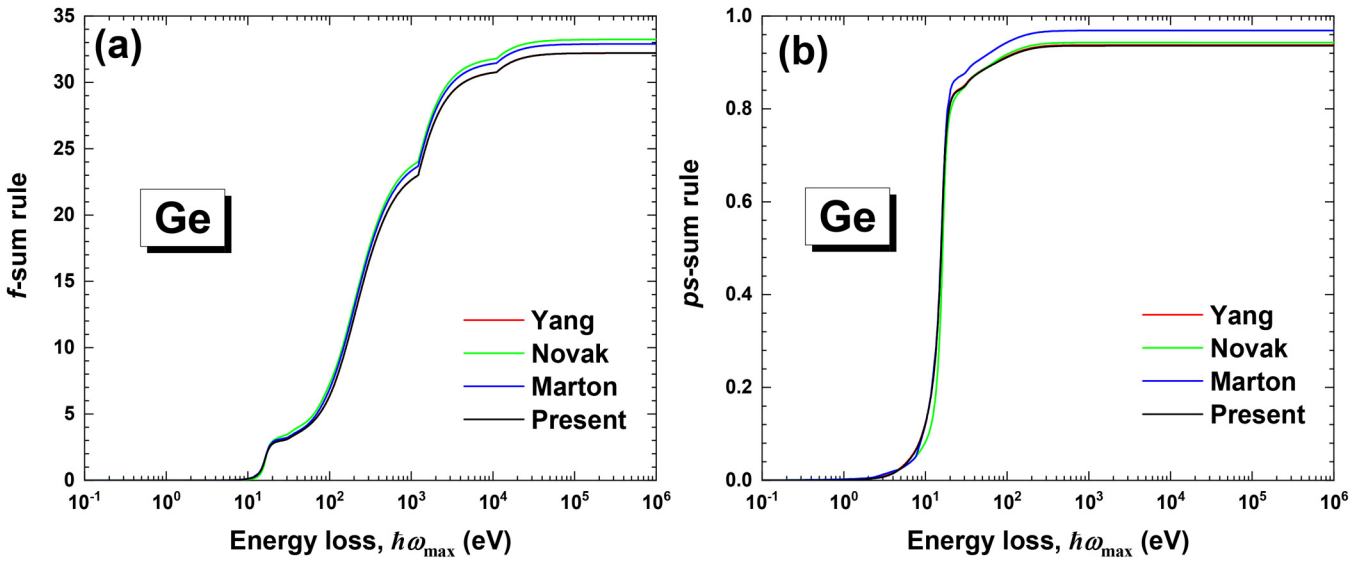

FIG. 3. Comparison of (a) *f*-sum and (b) *ps*-sum integrations for the four different ELFs.

were performed. The Monte Carlo computation was carried out on a parallel computer; for every simulation input, we have tracked the trajectories of 1×10^5 incident electrons as well as many times secondary electron cascades to derive SEY and BSC, hence the total electron yield (TEY) being the sum of SEY and BSC.

IV. RESULTS AND DISCUSSION

For the "Present-ELF" and work function value of 3.52 eV, the calculated SEY, BSC, and TEY curves in the primary energy range of 10 eV –10 keV with the 384 elastic cross section models are shown in Fig. 5. The calculated results were compared with the experimental data to check the range of uncertainty in yields due to elastic scattering models. It can be seen from the graphs that the yields can be affected significantly by the scattering potential model. As a result of inclusion of 384 elastic cross section models, our TEY results are in reasonable agreement with the experimental data of Bronstein and Fraiman for up to 4 keV [Fig. 5(c)], who employed *in situ* deposition technique to prepare a clean surface for the measurement of electron yields.[96] Reimer and Tollkamp have measured TEY in the higher energy range above 1 keV, and their data are much greater than this calculation.[97] The calculated mean and minimum BSC curves show reasonable agreement with the experimental datasets of Bishop,[98] Drescher,[99] Hunger and Küchler,[100] and Palmberg.[101] One can also see that there is a significant difference with the BSC of El Gomati *et al.*[102] for which the authors suspect that there could still be oxygen or carbon contamination on the sample surface. The previous studies[17–19] have already shown that the BSC value will be decreased whenever there exists a contamination of lower atomic number elements on the sample surface.

The case for SEY is quite different from BSC. The experimental SEY data[10,96,97,101,103–105] in Joy's database are rather widely dispersed, and the dispersion is larger as compared to other materials. Palmberg's SEY data show the greater values, whereas Bronstein's data present the smaller values. The data from Johnson and McKay,[103] Kanaya and Ono,[104] and Whetten[105] are in between and more close to Palmberg's data. However, Walker's data[10] are smaller than Bronstein's data[96] below 300 eV and greater above 300 eV perhaps due to residual contamination even for the "cleaned surface." The information that is currently known in the literature on the impact of contamination on SEY is, however,

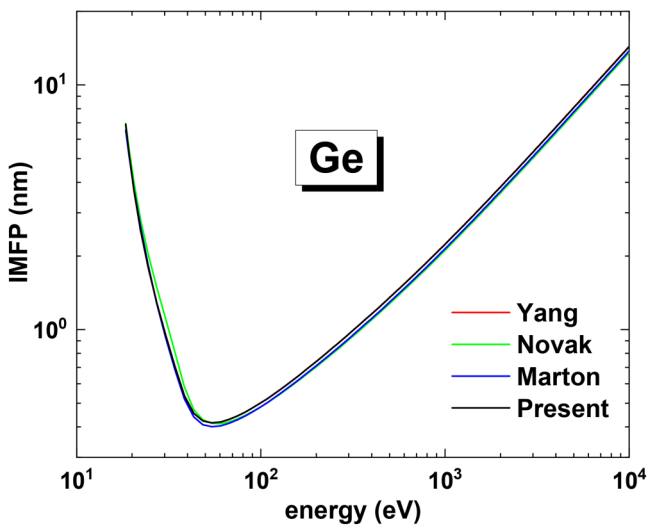

FIG. 4. Calculated IMFPs by FPA model with the four different ELFs.

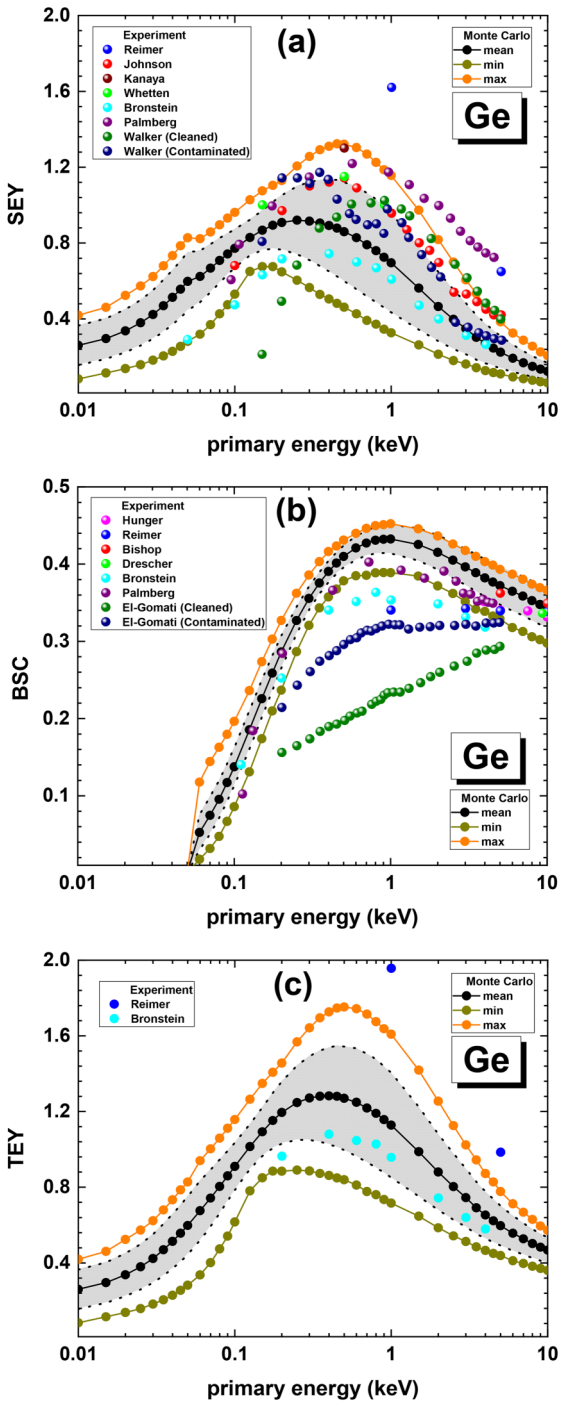

FIG. 5. Comparison of the simulations by using 384 elastic scattering potentials with experimental data for (a) SEY, (b) BSC, and (c) TEY. The FPA model, "ELF-Present" data, and work function of 3.52 eV are used to calculate the simulation results. The black, green, and orange colors represent, respectively, the mean, the minimum, and the maximum values of the 384 yield data at each energy. The gray area represents the standard deviation range.

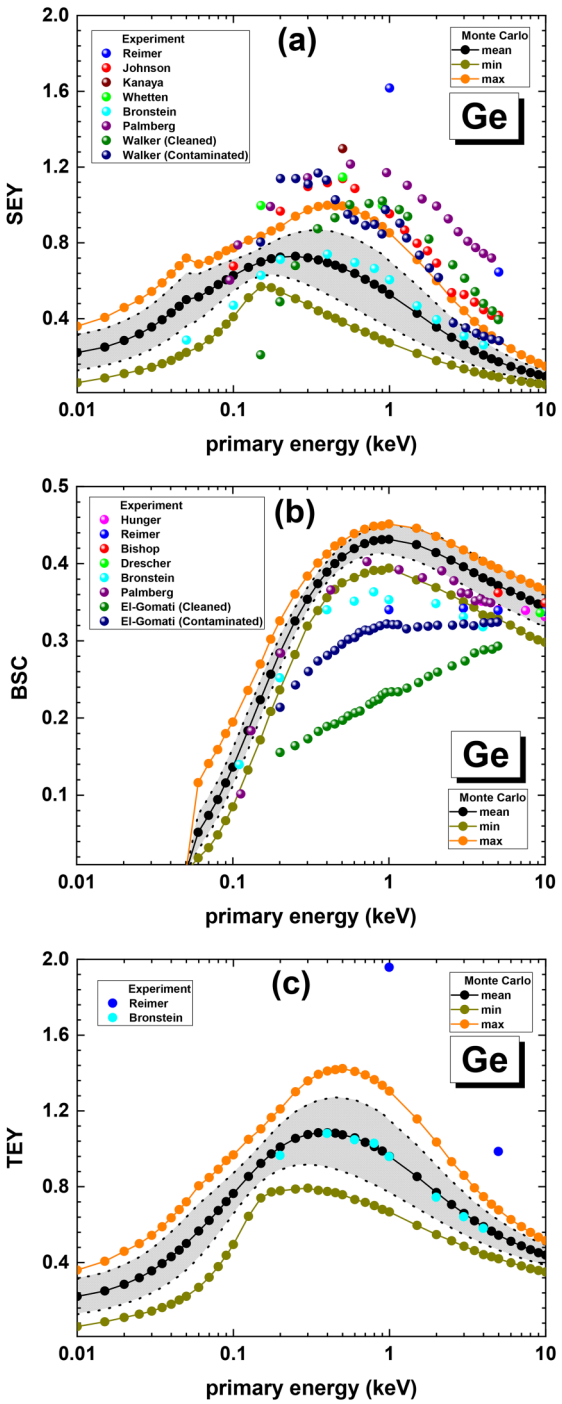

FIG. 6. Comparison of the simulations by using 384 elastic scattering potentials with experimental data for (a) SEY, (b) BSC, and (c) TEY. The FPA model, "ELF-Present" data, and work function of 4.16 eV are used to calculate the simulation results. The black, green, and orange colors represent, respectively, the mean, the minimum, and the maximum values of the 384 yield data at each energy. The gray area represents the standard deviation range.

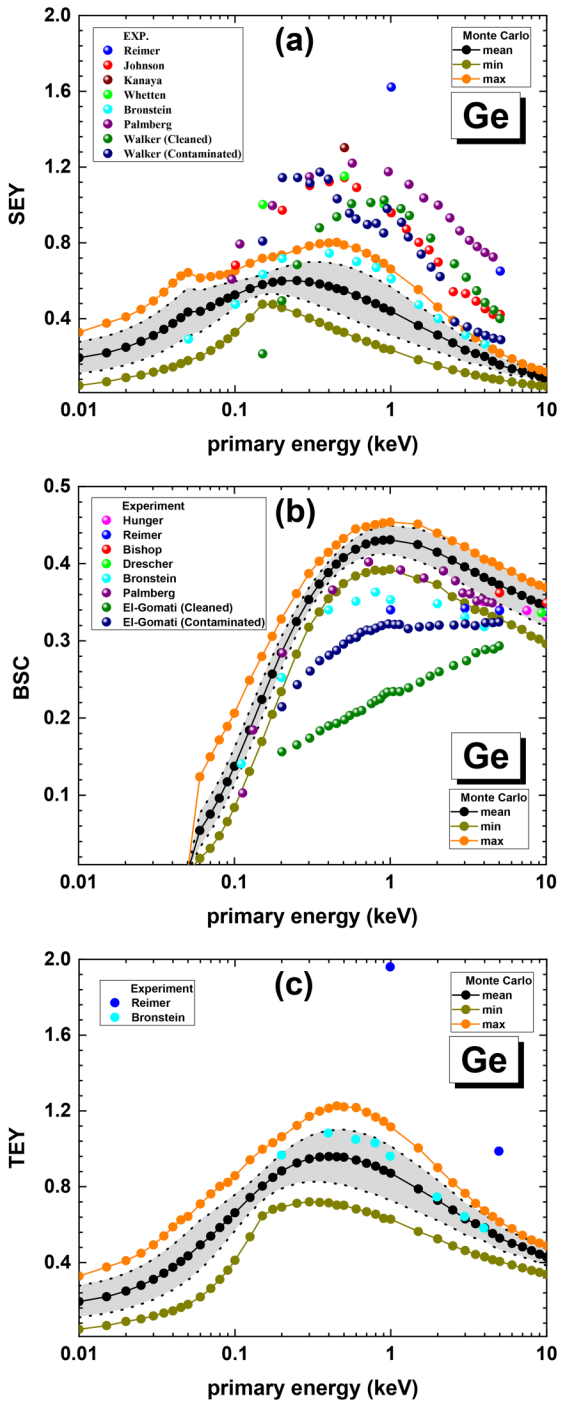

FIG. 7. Comparison of the simulations by using 384 elastic scattering potentials with experimental data for (a) SEY, (b) BSC, and (c) TEY. The FPA model, "ELF-Present" data, and a work function of 4.83 eV are used to calculate the simulation results. The black, green, and orange color represents, respectively, the mean, the minimum, and maximum values of the 384 yield data at each energy. The gray area represents the standard deviation range.

questionable. Several experiments show that SEY for surfaces that are as-inserted with oxygen or carbon on their surface[10,106] is lower than that of the clean surface. However, other studies have indicated that the cleaned surface had lower SEY values than the sample as-received.[107,108] A recent theoretical study investigated the most likely source of increase in SEY for adsorbed surfaces, despite the possibility of an increase in the work function. Both oxygen and carbon atoms affect the IMFP and density of states via chemical adsorption.[109] Because of the combined impacts of the change in the density of states and work function, a systematic inaccuracy in the measurement of SEY data could result from even minute amount of contaminants on the surface. Furthermore, ion sputtering of the surface can enhance surface roughness and alter the secondary electron emission.[110]

Figures 6 and 7 present the calculation results of SEY, BSC, and TEY when the work function is taken as 4.16 and 4.83 eV, respectively, and comparison with the experimental data. Together with Fig. 5, it is easily found that the simulated SEY and TEY values are reduced for the elevated work function value. The maximum SEY and TEY values correspond to the minimum work function value (3.52 eV). Experimentally, this also manifests as the source of measurement uncertainty due to contamination.

Furthermore, the theoretical uncertainty element of the scattering potential model has been taken into account in the current methodology. We have considered 384 elastic scattering potential models, using the FPA model and "ELF-present." In each figure of Figs. 5–7, we change only the elastic scattering potential model while keeping other parameters fixed. One may find that the scattering potential also greatly affects the simulation results of SEY and TEY, but weakly for BSC, whereas for SEY, the minimum and the maximum curves do not correspond to certain unique potentials. Different potential models result in the maximum SEY in different primary energy regions and so does the minimum SEY. One

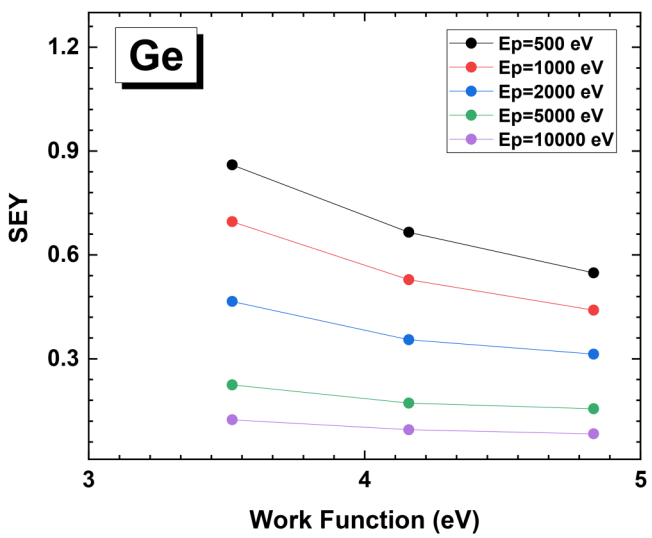

FIG. 8. Effect of work functions on SEY at different primary energies.

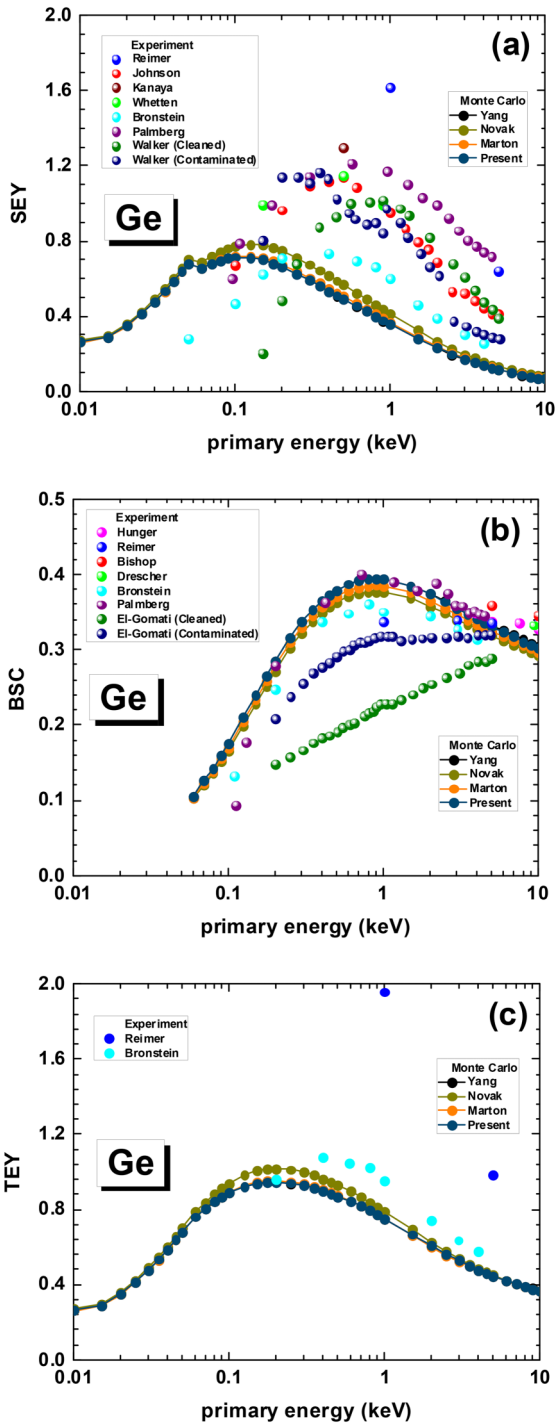

FIG. 9. Comparison of the simulations by using four different ELFs, "ELF-Yang," "ELF-Novak," "ELF-Marton," and "ELF-Present," with experimental data for (a) SEY, (b) BSC, and (c) TEY. The FPA model, "No. 42001" elastic potential, and a work function of 4.16 eV are used to calculate the simulation results.

may find a few suitable models that can fit the results in the entire range if accurate experimental data were known. In the figures, the shaded area represents the standard deviation from the simulated 384 models. The SEY curve changes abruptly at 50 eV because the backscattered electrons are counted as secondary electrons by definition. One can see from Figs. 7(a) and 7(c) that, for the work function of 4.16 eV, the simulated mean SEY and TEY values closely agree with Bronstein's measurement[96] within the range of theoretical uncertainty.

Figure 8 shows the effect of work function on SEY for different primary energies of 500, 1000, 2000, 5000, and 10 000 eV. For each primary energy, the SEY decreases slowly with the increase in the work function.

Figure 9 shows that the calculated electron emission yields by using different ELF datasets while fixing the scattering potential model and work function value. The elastic scattering cross section used in our calculation was computed from a particular scattering potential labeled "42 001." Here, each digit has a specific meaning: the first digit "4" represents Helm's uniform–uniform nuclear charge distribution model, the second digit "2" represents the Thomas–Fermi–Dirac electron distribution model, the third digit "0" indicates the absence of an exchange potential, the fourth digit "0" indicates the lack of a correlation-polarization potential, and the fifth digit "1" implies the utilization of the bound atom muffin-tin model. The "ELF-Novak" produces higher SEY/TEY values than the remaining ELFs. Although the "ELF-Yang" and the "ELF-Present" have very different values below the bandgap but show almost the same electron emission yields because the energy loss below the bandgap has negligible contribution to the transport of secondary electrons. Therefore, the different ELF datasets slightly effect the simulation results. Our results are in good agreement with the experimental data of Bronstein[96] for SEY, BSC, and TEY. In the case of BSC, experimental data of Reimer[97] and Palmberg[101] also align well with our simulated results.

V. CONCLUSION

The existing experimental data of measured electron emission yields (SEY, BSC, and TEY) show significant dispersion, especially for SEY. This dispersion is mainly due to the varied physical and chemical properties of the sample surface during measurements. Consequently, available experimental databases cannot provide accurate and reliable electron emission yield data for validating theoretical models of electron–matter interaction. In this study, we have conducted a calculation of electron emission yields from germanium together with theoretical uncertainty. We have considered several factors, such as elastic potential models for calculating electron elastic scattering cross sections, optical ELF datasets for calculating electron inelastic scattering cross sections, work function values, in the Monte Carlo simulations. Our simulation results indicate that the theoretical uncertainty of BSC is small. However, for SEY and TEY, the uncertainty is significant, with the work function and elastic potential as the main contributing factors. For 384 elastic potential models, the value of SEY varies from 0.46 to 1.32 at a primary energy of 0.5 keV, with a standard deviation of 0.26 when the work function is 3.52 eV. In the case of 4.16 eV work function, the SEY ranges from 0.38 to 0.99 and the standard

deviation is 0.18, while for the 4.83 eV work function, the SEY is 0.32–0.79 with 0.13 standard deviation. A notable finding from our study is that our theoretical SEY calculations are lower than the published experimental SEY data in Joy's database. This suggests that the previously measured SEY data may contain serious systematic errors and are likely overestimated. This work serves as a foundation for future efforts in establishing a theoretical database for electron emission. In this study of electron emission from germanium, we gained valuable insights into the uncertainties associated with the calculated SEY due to theoretical modeling. However, it is necessary to note that the systematic uncertainties, such as surface effects in theoretical modeling and limitations of the dielectric function theory, were not considered. The present study serves as a step to further research to move further for the comprehensive quantification of electron emission processes.

ACKNOWLEDGMENTS

Y. B. Zou acknowledges the National Natural Science Foundation of China (NNSFC) (Grant No. 12464037) and the Natural Science Foundation of Xinjinag Uygur Autonomous Region (Grant No. 2022D01A223). S. F. Mao acknowledges the National MCF Energy R&D Program of China (Grant No. 2019YFE03080500) and the Collaborative Innovation Program of Hefei Science Centre, CAS (Grant No. 2022HSC-CIP010). We thank Professor H. M. Li and the supercomputing center of USTC for the support of parallel computing.

AUTHOR DECLARATIONS

Conflict of Interest

The authors have no conflicts to disclose.

Author Contributions

H. I. Imtiaz: Formal analysis (equal); Investigation (equal); Software (equal); Visualization (equal); Writing – original draft (equal); Writing – review & editing (equal). **Y. B. Zou:** Funding acquisition (equal); Investigation (equal). **S. F. Mao:** Funding acquisition (supporting); Methodology (supporting); Software (supporting). **M. S. S. Khan:** Investigation (supporting). **Z. J. Ding:** Conceptualization (equal); Funding acquisition (equal); Methodology (equal); Project administration (equal); Software (equal); Supervision (equal); Visualization (equal); Writing – review & editing (equal).

DATA AVAILABILITY

The data that support the findings of this study are available from the corresponding authors upon reasonable request.

REFERENCES

[1]L. Austin and H. Starke, "On the reflection of cathode rays and a related new phenomenon of secondary emission," Ann. Phys. **314**, 271–292 (1902).
[2]L. Reimer, *Scanning Electron Microscopy: Physics of Image Formation and Microanalysis* (Springer, 1985).
[3]S. Pendyala, J. W. McGowan, P. H. R. Orth, and P. W. Zitzewitz, "Detection of low energy positrons using spiraled electron multipliers," Rev. Sci. Instrum. **45**, 1347 (1974).
[4]V. R. Manfrinato, L. Zhang, D. Su, H. Duan, R. G. Hobbs, E. A. Stach, and K. K. Berggren, "Resolution limits of electron-beam lithography toward the atomic scale," Nano Lett. **13**, 1555–1558 (2013).
[5]S. R. Zandi, A. Vastesson, W. Guo, W. Van Der Wijngaart, and T. Haraldsson, "E-beam nanostructuring and direct click biofunctionalization of thiol–ene resist," ACS Nano **12**, 9940–9946 (2018).
[6]R. Cimino, I. R. Collins, M. A. Furman, M. Pivi, F. Ruggiero, G. Rumolo, and F. Zimmermann, "Can low-energy electrons affect high-energy physics accelerators?," Phys. Rev. Lett. **93**, 014801 (2004).
[7]W. Jiang, K. Woolverton, J. Dickens, and M. Kristiansen, "High power microwave generation by a coaxial virtual cathode oscillator," IEEE Trans. Plasma Sci. **27**, 1538–1542 (1999).
[8]H. Bruining, *Physics and Applications of Secondary Electron Emission* (McGraw-Hill, New York, 1954).
[9]A. E. Vladar, M. T. Postek, and R. Vane, "Active monitoring and control of electron beam induced contamination," Proc. SPIE **4344**, 835–843 (2001).
[10]C. G. H. Walker, M. M. El-Gomati, A. M. D. Assa'd, and M. Zadražil, "The secondary electron emission yield for 24 solid elements excited by primary electrons in the range 250–5000 eV: A theory/experiment comparison," Scanning **30**, 365–380 (2008).
[11]M. Hugenschmidt, K. Adrion, A. Marx, E. Müller, and D. Gerthsen, "Electron-beam-induced carbon contamination in STEM-in-SEM: Quantification and mitigation," Microsc. Microanal. **29**, 219–234 (2023).
[12]D. C. Joy, "A database on electron-solid interactions," Scanning **17**, 270–275 (1995).
[13]A. J. Dekker, "Secondary electron emission," Solid State Phys. **6**, 251–311 (1958).
[14]Z. J. Ding, X. D. Tang, and R. Shimizu, "Monte Carlo study of secondary electron emission," J. Appl. Phys. **89**, 718–726 (2001).
[15]B. D. Mehnaz and Z. J. Ding, "Exploring the absolute yield curve of secondary electrons using machine learning methods," Phys. Chem. Chem. Phys. **25**, 17238–17256 (2023).
[16]S. H. Kim, M. G. Pia, T. Basaglia, M. C. Han, G. Hoff, C. H. Kim, and P. Saracco, "Validation test of Geant4 simulation of electron backscattering," IEEE Trans. Nucl. Sci. **62**, 451–479 (2015).
[17]A. Hussain, L. Yang, S. Mao, B. Da, K. Tőkési, and Z. J. Ding, "Determination of electron backscattering coefficient of beryllium by a high-precision Monte Carlo simulation," Nucl. Mater. Energy **26**, 100862 (2021).
[18]L. Yang, A. Hussain, S. Mao, B. Da, K. Tőkési, and Z. J. Ding, "Electron backscattering coefficients of molybdenum and tungsten based on the Monte Carlo simulations," J. Nucl. Mater. **553**, 153042 (2021).
[19]H. I. Imtiaz, M. S. S. Khan, A. Hussain, S. F. Mao, Y. B. Zou, and Z. J. Ding, "Electron backscattering coefficients for Cr, Co, and Pd solids: A Monte Carlo simulation study," J. Appl. Phys. **135**, 22 (2024).
[20]R. Shimizu and Z. J. Ding, "Monte Carlo modelling of electron-solid interactions," Rep. Prog. Phys. **55**, 487 (1992).
[21]D. C. Joy, *Monte Carlo Modeling for Electron Microscopy and Microanalysis* (Oxford University Press, 1995).
[22]M. Dapor, *Electron-Beam Interactions with Solids: Application of the Monte Carlo Method to Electron Scattering Problems* (Springer, 2003).
[23]M. Dapor, *Transport of Energetic Electrons in Solids: Computer Simulation with Applications to Materials Analysis and Characterization* (Springer, 2023).
[24]Z.-J. Ding, R. Shimizu, and K. Obori, "Monte Carlo simulation of x-ray spectra in electron probe microanalysis: Comparison of continuum with experiment," J. Appl. Phys. **76**, 7180–7187 (1994).
[25]X. Llovet, A. Moy, P. T. Pinard, and J. H. Fournelle, "Electron probe microanalysis: A review of recent developments and applications in materials science and engineering," Prog. Mater. Sci. **116**, 100673 (2021).
[26]N. Samoto and R. Shimizu, "Theoretical study of the ultimate resolution in electron beam lithography by Monte Carlo simulation, including secondary electron generation: Energy dissipation profile in polymethylmethacrylate," J. Appl. Phys. **54**, 3855–3859 (1983).
[27]X. Sun, Z. J. Ding, Q. R. Pu, H. M. Li, Z. Q. Wu, W. Q. Gu, and N. K. Kang, "Monte Carlo simulation of electron transmission through the scattering masks

with angular limitation for projection electron lithography," J. Appl. Phys. **92**, 3641–3646 (2002).
[28]M. Rommel, K. E. Hoffmann, T. Reindl, J. Weis, N. Unal, and U. Hofmann, "Benchmark test of Monte-Carlo simulation for high resolution electron beam lithography," Microelectron. Eng. **98**, 202–205 (2012).
[29]H. M. Li and Z. J. Ding, "Monte Carlo simulation of secondary electron and backscattered electron images in scanning electron microscopy for specimen with complex geometric structure," Scanning **27**, 254–267 (2005).
[30]Y. T. Yue, H. M. Li, and Z. J. Ding, "Monte Carlo simulation of secondary electron and backscattered electron images for a nanoparticle-matrix system," J. Phys. D: Appl. Phys. **38**, 1966–1977 (2005).
[31]J. S. Villarrubia, N. W. M. Ritchie, and J. R. Lowney, "Monte Carlo modeling of secondary electron imaging in three dimensions," Proc. SPIE **6518**, 65180K (2007).
[32]Y. G. Li, S. F. Mao, H. M. Li, S. M. Xiao, and Z. J. Ding, "Monte Carlo simulation study of scanning electron microscopy images of rough surfaces," J. Appl. Phys. **104**, 064901 (2008).
[33]P. Zhang, H. Y. Wang, Y. G. Li, S. F. Mao, and Z. J. Ding, "Monte Carlo simulation of secondary electron images for real sample structures in scanning electron microscopy," Scanning **34**, 145–150 (2012).
[34]Z.-J. Ding and R. Shimizu, "Monte Carlo simulation study of reflection electron energy loss spectroscopy spectrum," Phys. Rev. B **61**, 14128–14135 (2000).
[35]B. Da, S. F. Mao, G. H. Zhang, X. P. Wang, and Z. J. Ding, "Monte Carlo modeling of surface excitation in reflection electron energy loss spectroscopy spectrum for rough surfaces," J. Appl. Phys. **112**, 034310 (2012).
[36]N. Cao, B. Da, Y. Ming, S. F. Mao, K. Goto, and Z. J. Ding, "Monte Carlo simulation of full energy spectrum of electrons emitted from silicon in Auger electron spectroscopy," Surf. Interface Anal. **47**, 113–119 (2015).
[37]D. Emfietzoglou, G. Papamichael, and H. Nikjoo, "Monte Carlo electron track structure calculations in liquid water using a new model dielectric response function," Radiat. Res. **188**, 355–368 (2017).
[38]T. Koshikawa and R. Shimizu, "A Monte Carlo calculation of low-energy secondary electron emission from metals," J. Phys. D: Appl. Phys. **7**, 1303 (1974).
[39]J. P. Ganachaud and M. Cailler, "A Monte-Carlo calculation of the secondary electron emission of normal metals: I. The model," Surf. Sci. **83**, 498–518 (1979).
[40]H.-J. Fitting and J. Reinhardt, "Monte-Carlo simulation of keV-electron scattering in solid targets," Phys. Status Solidi A **88**, 245–259 (1985).
[41]D. C. Joy, "A model for calculating secondary and backscattered electron yields," J. Microsc. **147**, 51–64 (1987).
[42]Z. J. Ding and R. Shimizu, "Monte Carlo study of backscattering and secondary electron generation," Surf. Sci. **197**, 539–554 (1988).
[43]M. Kotera, "A Monte Carlo simulation of primary and secondary electron trajectories in a specimen," J. Appl. Phys. **65**, 3991–3998 (1989).
[44]Z. J. Ding, "Fundamental studies on the interactions of kV electrons with solids for applications to electron spectroscopies," Ph.D. dissertation (University of Osaka, 1990).
[45]M. Dapor, "Monte Carlo simulation of backscattered electrons and energy from thick targets and surface films," Phys. Rev. B **46**, 618 (1992).
[46]Z. J. Ding and Z. Q. Wu, "A comparison of Monte Carlo simulation of electron scattering and x-ray production in solids," J. Phys. D: Appl. Phys. **26**, 507–516 (1993).
[47]Z.-J. Ding, T. Nagatomi, R. Shimizu, and K. Goto, "Monte Carlo simulation of background in AES: A comparison with experiment," Surf. Sci. **336**, 397–403 (1995).
[48]Z.-J. Ding and R. Shimizu, "A Monte Carlo modeling of electron interaction with solids including cascade secondary electron production," Scanning **18**, 92–113 (1996).
[49]L. Van Kessel and C. W. Hagen, "Nebula: Monte Carlo simulator of electron-matter interaction," SoftwareX **12**, 100605 (2020).
[50]Q. Gibaru, C. Inguimbert, P. Caron, M. Raine, D. Lambert, and J. Puech, "Geant4 physics processes for microdosimetry and secondary electron emission simulation: Extension of MicroElec to very low energies and 11 materials (C, Al, Si, Ti, Ni, Cu, Ge, Ag, W, Kapton and SiO_2)," Nucl. Instrum. Methods Phys. Res. Sect., B **487**, 66–77 (2021).
[51]D. R. Penn, "Electron mean-free-path calculations using a model dielectric function," Phys. Rev. B **35**, 482 (1987).
[52]Z. J. Ding, H. M. Li, K. Goto, Y. Z. Jiang, and R. Shimizu, "Energy spectra of backscattered electrons in Auger electron spectroscopy: Comparison of Monte Carlo simulations with experiment," J. Appl. Phys. **96**, 4598–4606 (2004).
[53]Z. J. Ding, H. M. Li, X. D. Tang, and R. Shimizu, "Monte Carlo simulation of absolute secondary electron yield of Cu," Appl. Phys. A: Mater. Sci. Process. **78**, 585–587 (2004).
[54]E. D. Palik, *Handbook of Optical Constants of Solids*, 3rd ed. (Academic Press, 1998).
[55]M. Azzolini, T. Morresi, G. Garberoglio, L. Calliari, N. M. Pugno, S. Taioli, and M. Dapor, "Monte Carlo simulations of measured electron energy-loss spectra of diamond and graphite: Role of dielectric-response models," Carbon **118**, 299–309 (2017).
[56]H. Chen, Y. Zou, S. Mao, M. S. S. Khan, K. Tokesi, and Z. J. Ding, "Influence of energy loss function to the Monte Carlo simulated electron backscattering coefficient," Sci. Rep. **12**, 18201 (2022).
[57]B. Da, Y. Sun, S. F. Mao, Z. M. Zhang, H. Jin, H. Yoshikawa, and Z. J. Ding, "A reverse Monte Carlo method for deriving optical constants of solids from reflection electron energy-loss spectroscopy spectra," J. Appl. Phys. **113**, 214303 (2013).
[58]H. Xu, B. Da, J. Tóth, K. Tőkési, and Z. J. Ding, "Absolute determination of optical constants by reflection electron energy loss spectroscopy," Phys. Rev. B **95**, 195417 (2017).
[59]H. Xu, L. H. Yang, B. Da, J. Tóth, K. Tőkési, and Z. J. Ding, "Study of optical and electronic properties of nickel from reflection electron energy loss spectra," Nucl. Instrum. Methods Phys. Res. Sect., B **406**, 475–481 (2017).
[60]H. Xu, L. H. Yang, J. Tóth, K. Tőkési, B. Da, and Z. J. Ding, "Absolute determination of optical constants of three transition metals using reflection electron energy loss spectroscopy," J. Appl. Phys. **123**, 043306 (2018).
[61]L. H. Yang, M. Menyhárd, A. Sulyok, K. Tőkési, and Z. J. Ding, "Optical properties and excitation energies of iridium derived from reflection electron energy loss spectroscopy spectra," Appl. Surf. Sci. **456**, 999–1003 (2018).
[62]L. H. Yang, K. Tőkési, J. Tóth, B. Da, H. M. Li, and Z. J. Ding, "Optical properties of silicon and germanium determined by high-precision analysis of reflection electron energy loss spectroscopy spectra," Phys. Rev. B **100**, 245209 (2019).
[63]L. H. Yang, J. M. Gong, A. Sulyok, M. Menyhárd, G. Sáfrán, K. Tőkési, and Z. J. Ding, "Optical properties of amorphous carbon determined by reflection electron energy loss spectroscopy spectra," Phys. Chem. Chem. Phys. **23**, 25335 (2021).
[64]T. F. Yang, R. G. Zeng, L. H. Yang, A. Sulyok, M. Menyhárd, K. Tőkési, and Z. J. Ding, "Energy loss function of samarium," Sci. Rep. **13**, 3909 (2023).
[65]Z. Li, J. M. Gong, B. Da, J. Tóth, K. Tőkési, R. G. Zeng, and Z. J. Ding, "Improved reverse Monte Carlo analysis of optical property of Fe and Ni from reflection electron energy loss spectroscopy spectra," Sci. Rep. **13**, 12480 (2023).
[66]Z. Li, J. M. Gong, Y. Harada, B. Da, R. G. Zeng, and Z. J. Ding, "Determination of the energy loss function of tungsten from reflection electron energy loss spectroscopy spectra," Res. Phys. **56**, 107247 (2024).
[67]T. F. Yang, J. Tóth, K. Tőkési, R. G. Zeng, and Z. J. Ding, "Optical properties of InSb derived from reflection electron energy loss spectroscopy spectrum," Vacuum **223**, 113097 (2024).
[68]J. M. Gong, X. Liu, L. H. Yang, A. Sulyok, Z. Baji, V. Kis, and Z. J. Ding, "Optical properties of hafnium-dioxide derived from reflection electron energy loss spectroscopy spectra," J. Alloys Compd. **1005**, 175744 (2024).
[69]Y. G. Li, Z. J. Ding, Z. M. Zhang, and K. Tokesi, "Monte Carlo calculation of electron Rutherford backscattering spectra and high-energy reflection electron energy loss spectra," Nucl. Instrum. Methods Phys. Res. Sect., B **267**, 215–220 (2009).
[70]A. Bernardini, *Bounding Uncertainty in Civil Engineering: Theoretical Background* (Springer Science & Business Media, 2010).
[71]R. A. Levine and L. M. Berliner, "Statistical principles for climate change studies," J. Clim. **12**, 564–574 (1999).
[72]H.-K. Chung, B. J. Braams, K. Bartschat, A. G. Csaszar, G. W. F. Drake, T. Kirchner, and J. Tennyson, "Uncertainty estimates for theoretical atomic and molecular data," J. Phys. D: Appl. Phys. **49**, 363002 (2016).

[73]W. S. M. Werner, K. Glantschnig, and C. Ambrosch-Draxl, "Optical constants and inelastic electron-scattering data for 17 elemental metals," J. Phys. Chem. Ref. Data **38**, 1013–1092 (2009).
[74]H. Kawano, "Effective work functions of the elements: Database, most probable value, previously recommended value, polycrystalline thermionic contrast, change at critical temperature, anisotropic dependence sequence, particle size dependence," Prog. Surf. Sci. **97**, 100583 (2022).
[75]K. G. McKay, "Secondary electron emission," Adv. Electron. Electron Phys. **1**, 65–130 (1948).
[76]E. M. Baroody, "A theory of secondary electron emission from metals," Phys. Rev. **78**, 780 (1950).
[77]N. F. Mott, "The scattering of fast electrons by atomic nuclei," Proc. R. Soc. London Ser., A **124**, 425–442 (1929).
[78]F. Salvat, A. Jablonski, and C. J. Powell, "ELSEPA—Dirac partial-wave calculation of elastic scattering of electrons and positrons by atoms, positive ions and molecules (new version announcement)," Comput. Phys. Commun. **261**, 107704 (2021).
[79]M. S. S. Khan, S. F. Mao, Y. B. Zou, D. B. Lu, B. Da, Y. G. Li, and Z. J. Ding, "An extensive theoretical quantification of secondary electron emission from silicon," Vacuum **215**, 112257 (2023).
[80]H. Shinotsuka, S. Tanuma, and C. J. Powell, "Calculations of electron inelastic mean free paths. XIII. Data for 14 organic compounds and water over the 50 eV to 200 keV range with the relativistic full Penn algorithm," Surf. Interface Anal. **54**, 534–560 (2022).
[81]D. Pines, *Elementary Excitations in Solids* (CRC Press, 1963).
[82]A. L. Fetter, *Quantum Theory of Many-Particle Systems* (McGraw-Hill, 1971).
[83]J. Lindhard, "On the properties of a gas of charged particles," R. Dan. Soc. Sci. Lett. Math.-Phys. Med. **28**, 1 (1954).
[84]R. H. Ritchie and A. Howie, "Electron excitation and the optical potential in electron microscopy," Philos. Mag. **36**, 463–481 (1977).
[85]B. L. Henke, E. M. Gullikson, and J. C. Davis, "X-ray interactions: Photoabsorption, scattering, transmission, and reflection at E = 50–30,000 eV, Z = 1–92," At. Data Nucl. Data Tables **54**, 181–342 (1993).
[86]D. E. Cullen, J. H. Hubbell, and L. Kissel, *EPDL97: The Evaluated Photo Data library97 Version* (Lawrence Livermore National Lab, 1997).
[87]M. Novák, L. Kövér, S. Egri, I. Cserny, J. Tóth, D. Varga, and W. Drube, "A simple statistical model for quantitative analysis of plasmon structures in XPS and Auger spectra of free-electron-like materials," J. Electron Spectrosc. Relat. Phenom. **163**, 7–14 (2008).
[88]L. Marton and J. Toots, "Optical properties of germanium in the far ultraviolet," Phys. Rev. **160**, 602 (1967).
[89]B. L. Henke, P. Lee, T. J. Tanaka, R. L. Shimabukuro, and B. K. Fujikawa, "Low-energy x-ray interaction coefficients: Photoabsorption, scattering, and reflection: E = 100–2000 eV Z = 1–94," At. Data Nucl. Data Tables **27**, 1–144 (1982).
[90]E. Shiles, T. Sasaki, M. Inokuti, and D. Y. Smith, "Self-consistency and sum-rule tests in the Kramers-Kronig analysis of optical data: Applications to aluminum," Phys. Rev. B **22**, 1612 (1980).
[91]G. D. Mahan, *Many-Particle Physics* (Springer, 2013).
[92]C. Cohen-Tannoudji, B. Diu, and F. Laloe, *Quantum Mechanics 1* (Wiley, 1977).
[93]ISO-JCGM 100, *Evaluation of Measurement Data-Guide to the Expression of Uncertainty in Measurement* (Int Organ Stand Geneva ISBN, 2008).
[94]ISO-JCGM 101, *Guide to the Expression of Uncertainty in Measurement* (Int Organ Stand Geneva ISBN, 2008).
[95]P. R. G. Couto, *Theory and Applications of Monte Carlo Simulations* (IntechOpen, 2013).
[96]I. M. Bronstein and B. S. Fraiman, *Vtorichnaya Elektronnaya Emissiya (Secondary Electron Emission)* (Nauka, Moskva, 1969).
[97]L. Reimer and C. Tollkamp, "Measuring the backscattering coefficient and secondary electron yield inside a scanning electron microscope," Scanning **3**, 35–39 (1980).
[98]H. E. Bishop, "Electron scattering and x-ray production," Ph.D. dissertation (University of Cambridge, 1966).
[99]H. Drescher, L. Reimer, and H. Seidel, "Backscattering and secondary electron emission of 10–100 keV electrons in scanning electron microscopy," Z. Angew. Phys. **29**, 331–336 (1970).
[100]H. J. Hunger and L. Küchler, "Measurements of the electron backscattering coefficient for quantitative EPMA in the energy range of 4 to 40 keV," Phys. Status Solidi A **56**, K45–K48 (1979).
[101]P. W. Palmberg, "Secondary emission studies on Ge and Na-covered Ge," J. Appl. Phys. **38**, 2137–2147 (1967).
[102]M. M. El Gomati, C. G. H. Walker, A. M. D. Assa'd, and M. Zadražil, "Theory experiment comparison of the electron backscattering factor from solids at low electron energy (250–5000 eV)," Scanning **30**, 2–15 (2008).
[103]J. B. Johnson and K. G. McKay, "Secondary electron emission from germanium," Phys. Rev. **93**, 668 (1954).
[104]K. Kanaya and S. Ono, "Interaction of electron beam with the target in scanning electron microscope," SEM **1982**, 6.
[105]N. R. Whetten, "Cleavage in high vacuums of alkali halide single crystals-electron emission," J. Appl. Phys. **35**, 3279–3282 (1964).
[106]J. Chen, E. Louis, J. Verhoeven, R. Harmsen, C. J. Lee, M. Lubomska, and F. Bijkerk, "Secondary electron yield measurements of carbon covered multilayer optics," Appl. Surf. Sci. **257**, 354–361 (2010).
[107]V. Petit, M. Taborelli, H. Neupert, P. Chiggiato, and M. Belhaj, "Role of the different chemical components in the conditioning process of air exposed copper surfaces," Phys. Rev. Accel. Beams **22**, 083101 (2019).
[108]T. A. Malik, "Secondary electron yield measurements on materials of interest to vacuum electron communication devices," M.S. dissertation (University of New Mexico, 2020).
[109]M. Brown, L. Diaz, A. Aslan, M. Sanati, S. Portillo, E. Schamiloglu, and R. P. Joshi, "Carbon-oxygen surface formation enhances secondary electron yield in Cu, Ag and Au," Sci. Rep. **12**, 15808 (2022).
[110]N. Balcon, D. Payan, M. Belhaj, T. Tondu, and V. Inguimbert, "Secondary electron emission on space materials: Evaluation of the total secondary electron yield from surface potential measurements," IEEE Trans. Plasma Sci. **40**, 282–290 (2012).